Capability of DFIGs to Provide Reactive Power Support and Low Voltage Ride Through in Hybrid Wind Farms with FSIGs

Bruce Bartlett Van Kirk III

A thesis

submitted in partial fulfillment of the

requirements for the degree of

Master of Science in Electrical Engineering

University of Washington

December 2012

Committee:

Richard D. Christie

Brandon Pierquet

Program Authorized to Offer Degree:

Electrical Engineering

University of Washington

Abstract

The Capability of DFIGs to Provide Reactive Power Support and Low Voltage Ride-Through in Hybrid Wind Farms with FSIGs

Bruce Bartlett Van Kirk III

Chair of the Supervisory Committee

Professor Richard D. Christie

Electrical Engineering

This thesis examines the low voltage event performance of hybrid wind farms containing both economical Fixed Speed Induction Generators (FSIGs) and the increasingly popular but more costly Doubly-Fed Induction Generators (DFIGs). Of particular interest is the ability of DFIGs, through manipulation of the converter control, to supply reactive power support to the point of common coupling, and low voltage ride through (LVRT) capability to the farm as a whole. The study employs a recently proposed vector-based current control scheme in the DFIGs for fast transient response. After constructing detailed models of the DFIG machine and this control scheme in the PSCAD power systems simulation software package, several scenarios are simulated and examined in an effort to observe the practical limits of the DFIGs reactive support capabilities. Specifically, the maximum ratio of FSIGs to DFIGs is investigated, as well as how DFIG rotor current limits and FSIG over-speed relays affect these ratios. The motivation of this work is the reduction in total cost of a hybrid wind farm.

Contents

I. INTRODUCTION

A. Wind Farms and Low Voltage Ride-Through

In recent decades, concerns regarding carbon emissions, climate change, and limitation of fossil fuels have led to a large increase in generation of electricity via renewable resources. Wind energy has been one of the more successful of these new additions to the generation pool. As penetration of wind energy has reached a substantial level (beyond 20% in some cases [1]), new power system operation issues have arisen as well. One of the most pressing issues relates to behavior of wind farms during low voltage events (faults).

When a fault occurs on the network, the drop in voltage it causes can have undesirable effects on wind turbines delivering power to the grid. These effects will be summarized in the next section, but in general, protection devices in the machines and/or plant act to disconnect the plant from the network. The resulting loss in active power generation makes it more difficult for the system to recover from the low voltage event. This problem led network administrators and regulating agencies to impose Low Voltage Ride-Through (LVRT) capability requirements on wind farms connected to the system [2]. While specifics vary from network to network, LVRT requirements generally specify a worst-case fault scenario (including % drop in voltage, duration, and recovery time) during which the wind plant must remain connected to the grid. The modifications in equipment and operation required to provide LVRT capability vary greatly, depending on the type of turbine(s) used in the farm. The two primary controllable components of the wind turbine are the blades (e.g. pitch angle) and the generator. This paper addresses LVRT with two types of generators, so discussion and performance analysis will focus on the generator types and their controls, rather than pitch angle control.

B. Electrical Machine Types

There are four types of electrical machines commonly used in wind turbines. 'Type I' machines are Fixed Speed squirrel-cage Induction Generators (FSIGs). FSIGs were the first popular generator used in large wind turbines, becoming commonplace in the 1990s [3]. FSIG stator windings are electrically connected to the grid, while the rotor is a simple 'squirrel-cage' construction of short-circuited die-cast rods with no brushes or slip rings. They are called fixed speed machines because through the operational range of wind speeds, the slip speed only changes by a few percent [4]. These machines' persisting popularity stems from their low capital cost, minimal maintenance requirements, and simplicity of operation. Their primary drawbacks are reduced efficiency and significant reactive power consumption [3].

'Type II' machines are variable speed induction machines, often with a wound rotor and variable rotor resistance [5]. While these machines offer increased flexibility and efficiency over Type I turbines, they constitute a small portion of the market and will not be further discussed in this thesis.

'Type IV' machines (Type III machines are discussed below) refer to configurations with induction or synchronous generators connected to the grid via a fully rated back-to-back AC-DC-AC converter. With this configuration, the turbine speed is allowed to vary greatly, enabling Maximum Power Point Tracking (MPPT), greater efficiency, and decoupled control of active and reactive power. While these machines have excellent functionality and efficiency, they are often deemed to be prohibitively expensive due to the large power electronics required in the converter [6]. Due to the lower occurrence of these machines, they are not considered here.

'Type III' machines are commonly referred to as Doubly-Fed Induction Generators (DFIGs), which have recently become the most popular generator in new construction [7].

DFIGs involve a wound rotor induction machine with the stator directly connected to the grid, but with the rotor windings also connected to the grid through a back-to-back converter. The advantage here is that the power electronics in the converter need only be a fraction of the size of a fully scaled converter (approximately 30%) [6]. The DFIG, like the Type IV machine, still offers decoupled control of active and reactive power, as well as increased efficiency when compared to Type I machines.

This thesis will examine wind farms containing both Type I (FSIG) and Type III (DFIG) machines which have become dominant in implementation today. We will observe the fault performance (i.e. LVRT) of plants using these two machines, both separately and in combination.

C. FSIGs and LVRT

With FSIG plants, the drop in terminal voltage that occurs during a fault causes the electromagnetic torque in the machine to drop, in other words largely removing the channel for real power output. Since the mechanical input (i.e. wind speed) remains the same, a power/torque mismatch begins, causing the rotor to rapidly accelerate [8]. If the fault is not cleared soon enough, the rotor will accelerate to a point beyond which it cannot stabilize and will continue to accelerate, even after fault clearing. Over-speed relays will trip to disconnect the machine from the network to prevent mechanical damage. In addition, FSIG reactive power consumption further increases during faults, making it even harder for the network to recover [9].

In recent years, the increase in wind generation construction and the LVRT regulations that arose have led to much research on LVRT approaches. The most popular solution for FSIG wind farms involves one of several FACTS (Flexible AC Transmission System) devices for fast reactive power compensation during faults. These include switched capacitors, static var

compensators (SVCs), and STATCOMs (Static Compensators) [9]. These devices are installed at or near the wind farm site, and upon fault detection will activate to inject an amount of reactive power sufficient to allow the farm to remain stable and connected to the network. While these devices have been proven in theory and in practice, they come at a significant cost, offsetting the economic benefit of FSIG machines.

D. DFIGs and LVRT

DFIGs exhibit very different behavior during faults, and thus their LVRT problems and solutions are unique as well. When a fault occurs on the network adjacent to a DFIG, the change in stator flux is reflected on the rotor windings, which can cause rotor currents that far exceed the rated values [10]. Even before LVRT requirements, this was an issue in DFIGs when considering machine safety. The common solution, referred to as a 'crowbar', essentially short circuits the rotor windings to prevent excessive currents. However, this also effectively disables the machine disconnects it from the grid, so in itself the crowbar is not an effective aid in enabling LVRT.

FACTS devices can be used with DFIGs in the same way they are with FSIGs to provide LVRT capability, but there is again the added cost dilemma. In recent years, many papers have been published that propose manipulating the conventional control schemes in the rotor-side and grid-side converters of the DFIG to achieve various functionalities. An extensive research survey of such approaches is presented in [11]. Of particular interest for this thesis are control approaches (for the DFIG back-to-back converter) to enable LVRT without any additional equipment. One early example was presented in [12], but had limited effectiveness with some fault scenarios [13]. More complex approaches were developed in [13], [14], [15], and [16].

With all converter control schemes, a major consideration is whether the targeted functionality operates during steady state or transients. Specifically, those control schemes

aiming to achieve successful transient performance (e.g. during a fault) often encounter difficulties in realizing fast response. This is because the control approaches often depend on accurate real-time measurement or estimation of the stator flux which is difficult to obtain [12]. In [17], the authors propose a novel control approach for the rotor and grid-side converters that uses a virtual grid flux-oriented reference frame in place of the conventional stator-flux oriented frame. In addition, they propose vector-based multi-level hysteresis comparators to generate the converter firing signals. These two modifications to the conventional DFIG control approach enable greatly improved transient performance, including for LVRT.

E. Hybrid Wind Farms

One proposed solution to providing LVRT capability to FSIGs in wind farms, discussed in [18], is to use some proportion of permanent magnet synchronous generator machines with full scaled converters (Type IV) in the farm as well. In [19], performance of these so-called 'hybrid wind farms' utilizing Type I and Type IV machines is compared to farms using only DFIGs. Both of these papers develop LVRT strategies for the hybrid farms. Despite a lack of significant research on the topic, there may be some economic and operational potential in hybrid wind farms utilizing more than one type of machine. This is especially true when the term 'wind farm' can include two or more proximate projects. Wind sites are often developed in phases or sub-sites [20], and market trends can result in different machine types being used in each site. In these cases, and in completely new construction projects, hybrid wind farms potentially offer economic solutions to satisfying LVRT and other regulatory connection requirements.

F. DFIGs Providing Reactive Power Support in Hybrid Wind Farms

In [8], hybrid wind farms comprised of FSIGs and DFIGs are investigated. This paper was the first and only example found in the literature that demonstrated using DFIGs' reactive power control capability to provide LVRT for adjacent FSIGs. The improved transient response of the controller introduced in [17] is employed to allow the DFIGs in the farm to inject reactive power at fault onset and support the farm through the fault. However, the paper only allows the rotor-side converter to participate in reactive power support, neglecting the potential of the grid-side converter. Moreover, the paper only considers a case with a large ratio of DFIGs to FSIGs. Lastly, the fault scenario considered in the paper is not as severe as the worst-case scenario specified in the U.S. Federal Energy Regulatory Commission's (FERC's) low voltage ride through requirement. This thesis expands on the work in [8] by addressing these issues, and further developing the proposed control algorithm. For the remainder of the paper, 'hybrid wind farms' refer to those comprised of DFIGs and FSIGs.

II. DESCRIPTION OF STUDY CASE

A. Network Model

In order to examine the low voltage response of FSIG, DFIG, and hybrid wind farms, the model in Figure 1 was constructed. For ease in modeling and to ensure reasonable simulation time, the DFIG and FSIG portions of the hybrid wind farm are each modeled as single machine. Wind speed is modeled as constant since its rate of change is typically negligible when considering transient scenario time frames. Due to the sensitivity of tuning parameters (especially in the numerous PI controllers of the converter control), the DFIG rated power output is held at 1MW. Multiple ratings of FSIG power output will be examined. Each machine generates at 690V and is stepped up to 34kV via transformer. Trunk line impedances are

considered negligible here relative to the machine transformers, though in future work modeling multiple discrete machines they would be included. The wind farm bus or point of common coupling (PCC) is connected to the grid via a transmission line, which is modeled as a simple impedance. The grid is modeled as an infinite bus, represented in simulation as an ideal voltage source. Machine and impedance data are taken from the PSCAD models which are based on real devices. This data is given in the appendix.

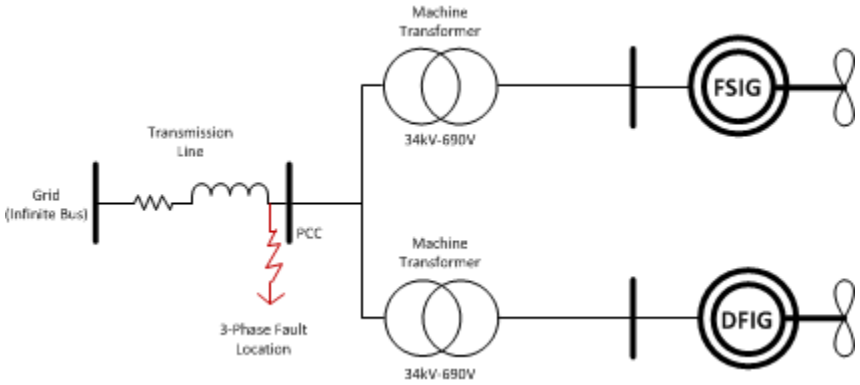

Figure 1: Network Model.

B. Fault Scenario

Comprehensive studies involving LVRT and faults typically consider multiple fault scenarios. Fault type (symmetric/asymmetric), location, impedance, and duration all have significant effects on system dynamic response. This thesis examines a fault scenario as described in FERC'S LVRT specification. Figure 2 illustrates the worst case voltage profile at the point of common coupling for which wind farms must stay connected, as specified by FERC in [21]. Here we consider only a symmetric three-phase fault, but future work would also observe asymmetric (e.g. single line to ground) faults. In the study network model, the fault is applied directly at the PCC, which would be the worst case network fault location.

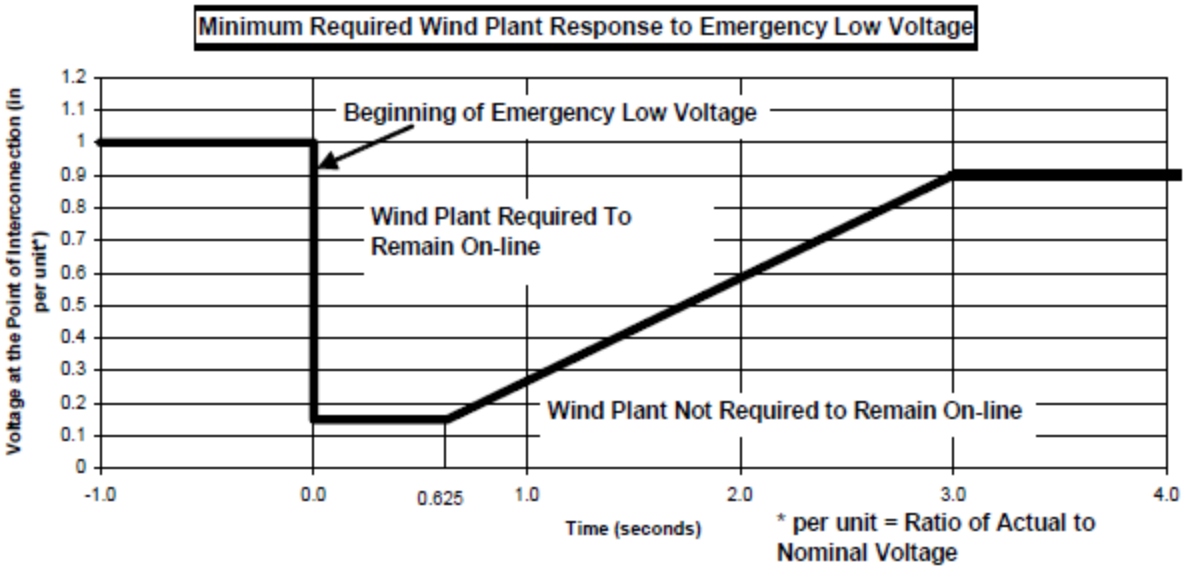

Figure 2: FERC Low Voltage Ride-Through Standard from [21].

In this study, the FERC fault scenario is modeled with a stepwise recovery to better suit the simulation package. This type of recovery is not unrealistic, as recovery is often accomplished via discrete actions (e.g. circuit breakers opening/closing). shows a plot of the simulated PCC voltage profile.

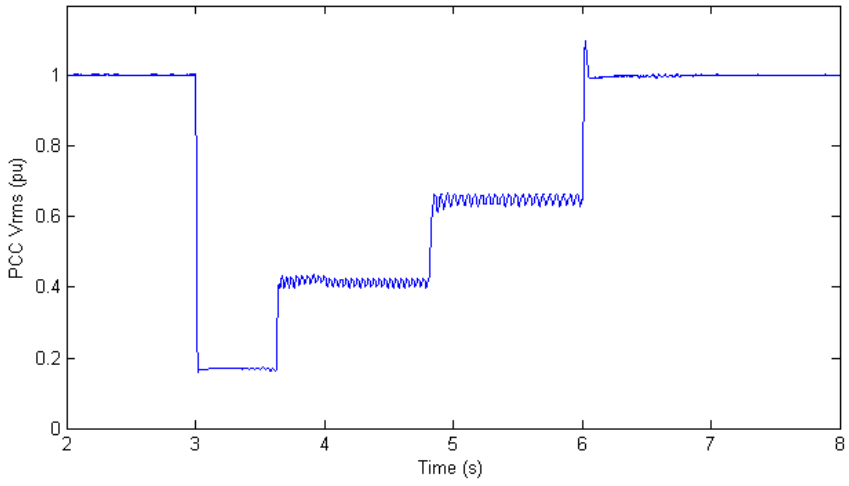

Figure 3: Simulation Fault Scenario PCC Voltage.

C. PSCAD/EMTDC

In order to analyze the LVRT performance of FSIG, DFIG and hybrid wind farms, this study set up time domain simulations of these farms through a fault scenario. When considering software packages to employ for simulation, two modeling capabilities were necessary. The first was the ability to model and simulate FSIGs and DFIGs both in steady state and during transients. The second was the ability to fundamentally modify the DFIG controller, including capability for coding the vector control algorithm and quadrature phase locked loop. PSCAD/EMTDC was chosen over Powerworld and PSS\E in particular for its built-in FSIG and wound rotor induction machine models, as well as for its extensive control design functionality.

III. FIXED SPEED INDUCTION MACHINE BEHAVIOR DURING FAULT

When a fault occurs on the network near a FSIG, the decreased voltage causes the electrical torque in the machine to decrease. As a result, the machine accelerates until the voltage is restored. During brief faults, the increase in angular velocity is small enough that the machine speed can return to its nominal range and remain online. However, if the fault is not cleared quickly enough, the increase in machine speed will reach a point where the machine becomes unstable and continues to accelerate even after fault clearing. Over-speed relays then act to disconnect the machine, thereby failing any low voltage ride-through requirement.

In order to illustrate this behavior, the test network was simulated using only FSIG machines. The fault scenario specified in the FERC LVRT standard is far too extreme for FSIGs to ride through without support. In order to observe the stability margin of unsupported FSIG LVRT, we will examine the response of the FSIG during faults where the PCC voltage

magnitude drops to only 0.4 pu. Figure 4 shows the shaft speed of FSIGs for faults of this magnitude and several durations.

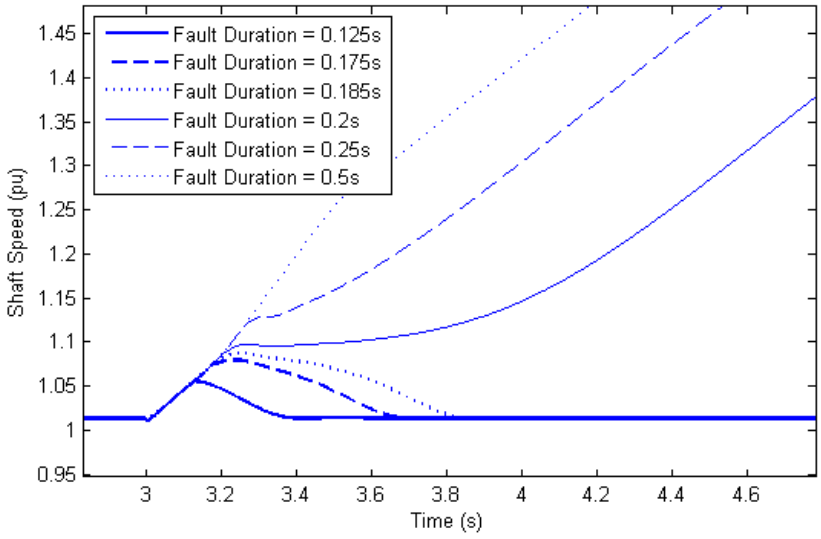

Figure 4: FSIG Shaft Speed during Voltage Drops to 0.4 pu.

After examining the plot, it is clear that for the shorter three faults, the speed increase is small enough that the machine is able to stabilize after fault clearing and return to normal speed. However, with the longer cases the machine continues to accelerate.

For further illustration, Figure 5 shows the real and reactive power outputs of the FSIG during the two most marginal cases.

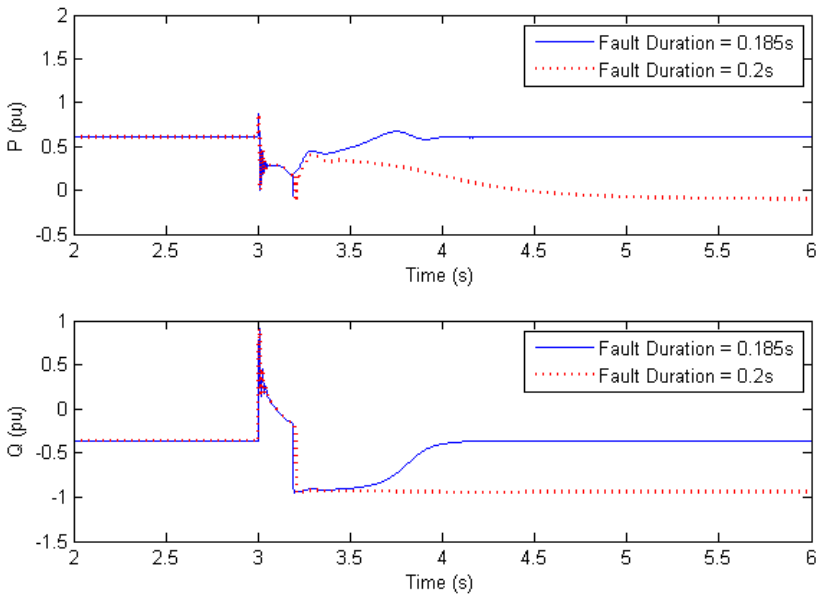

Figure 5: FSIG Real and Reactive Power during Voltage Drops to 0.4 pu.

In both cases, real power output is constant at its rated value before the fault, and drops in an abrupt transient at fault onset. In the stable (shorter duration) case, the real power is able to return to nominal after fault clearing, but in the unstable case the real power collapses. Observing the reactive power response, it can be observed that in both cases the machine is consuming a small amount of reactive power before the fault, as is standard for FSIGs. At fault onset there is a transient, and after fault clearing the reactive power absorption increases. For the stable case, the absorption is able to return to nominal, but the unstable case remains at the larger value. In both cases, the initial increase in reactive power absorption after fault clearing has the potential to inhibit network recovery.

It is clear from this brief analysis that FSIGs are only capable of riding through relatively minor faults if support is not present in some other form. In the next section we will outline the revised DFIG converter control scheme used in this study to observe DFIG LVRT behavior.

IV. DFIG VECTOR CONTROL USING HYSTERESIS-BASED CURRENT REGULATION

A. DFIG Structure and Control Summary

Figure 6, taken from [22], shows the schematic of a DFIG wind turbine. The machine is a wound rotor induction machine, with connections to the rotor windings brought out via slip rings and connected to the rotor-side converter (RSC). The Insulated Gate Bipolar Transistor (IGBT) based AC-DC RSC converts the three-phase voltage of the rotor to DC voltage which is coupled to a DC link capacitor. The DC link is also coupled to the DC side of the grid-side converter (GSC). Three-phase AC output of the GSC passes through a filter and is connected to the grid, along with the stator windings.

By manipulating the firing signals in the two converters, active and reactive power output can be separately controlled in each converter. In most approaches, the GSC converter is generally controlled to maintain the DC link voltage. The RSC is configured to adjust machine speed for maximum real power efficiency, and also to adjust reactive power input/output.

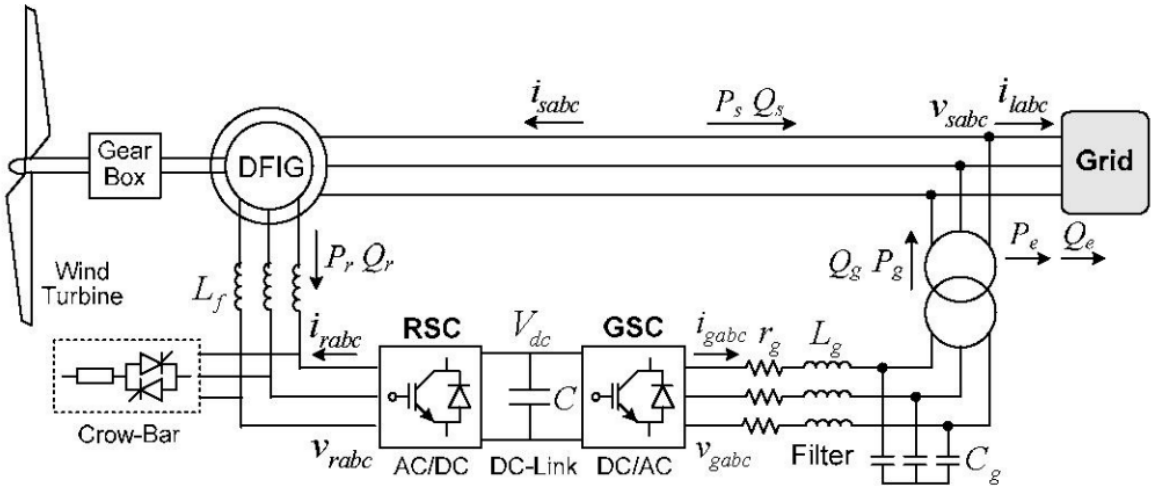

Figure 6: Schematic of DFIG Wind Turbine from [22].

This decoupled active and reactive power control is usually achieved by decomposing the rotor current signals into synchronous *dq* reference frame components and using conventional PI current control on the components. The rotating *dq* reference frame is synchronous with the

stator flux vector. As mentioned before, this approach works excellently for steady state operation, but not for transient operation because fast and accurate measurement or estimation of the stator flux angle is extremely important yet difficult to obtain [12].

This thesis uses an alternative approach from [17], in which a quadrature phase-locked loop is used to establish a virtual grid-flux oriented reference frame (GFOF) for synchronization, rather than the conventional stator-flux oriented frame. The virtual grid-flux vector is in quadrature with the grid voltage vector and can thus be extracted with a phase-locked loop. Figure 7, taken from [17], gives a graphical representation of GFOF, and shows why the stator flux (which is not exactly in quadrature with stator voltage) cannot be used for synchronization. Stator real and reactive power mismatch signals are passed to PI blocks which produce reference values for the GFOF *dq* rotor current components. These values are transformed into the rotor oriented reference frame (ROF) and passed to a vector-based hysteresis current regulator (VBHCR), which generates the RSC firing signals. The VBHCR's advantage over conventional hysteresis comparators lies in its ability to regulate effectively in steady-state and transient scenarios. These types of regulators have become popular in Voltage-Source Converters (VSCs) [17]. The GSC is also fitted with a similar VBHCR current regulator.

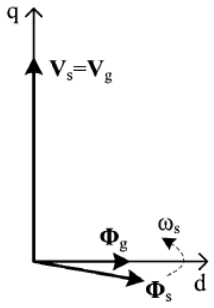

Figure 7: Vector Diagram of Synchronous Grid-Flux Oriented Reference Frame from [17]

Figure 8, taken from [17], gives a block diagram of the entire control algorithm. Real power reference calculation has been removed from this diagram as the method used in this

study to calculate reference power signals differs from that used in [17]. The details of each of the controller blocks are elaborated in the following sections.

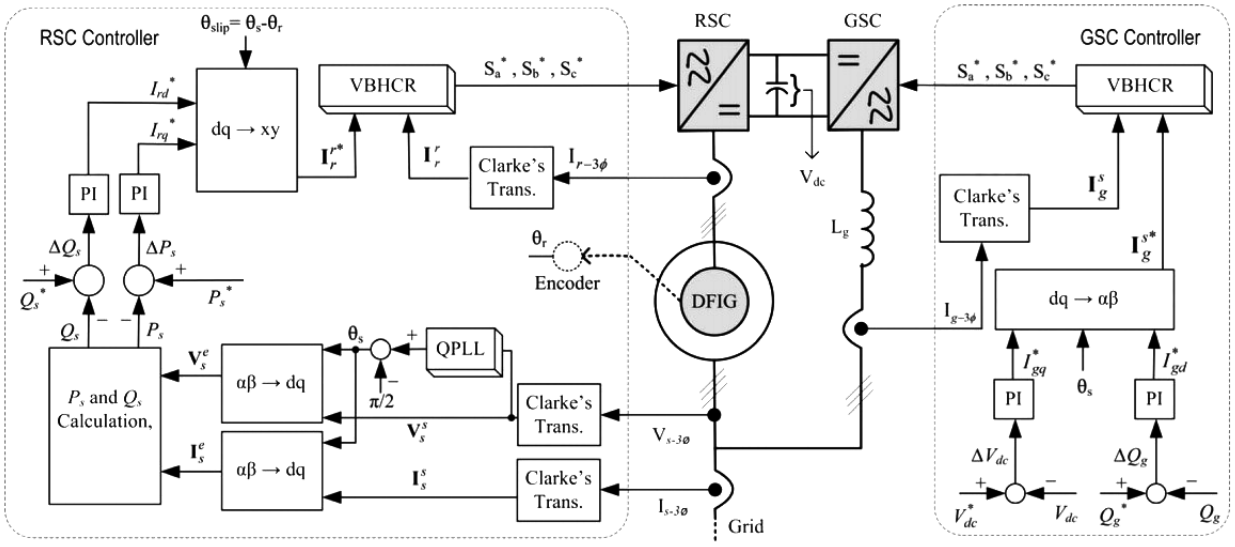

Figure 8: DFIG Converter Control Block Diagram Utilizing GFOF and VBHCR from [17].

B. Stationary Frame and Quadrature Phase-Locked Loop

The first objective in the control loop is to obtain a phase angle for the grid/stator voltage vector to be used for synchronization. While a standard phase-locked loop (with three-phase input) could be used, [17] explains that using a quadrature phase-locked loop (qPLL) provides a more robust solution, especially for transient and asymmetric scenarios. The inputs to the qPLL are the quadrature components of the stator/grid voltage signals in the stationary *αβ* reference frame. These are calculated via Clarke's Transform:

$$\begin{bmatrix} V_s^{\alpha} \\ V_s^{\beta} \end{bmatrix} = \begin{bmatrix} 1 & 0 \\ \frac{1}{\sqrt{3}} & \frac{2}{\sqrt{3}} \end{bmatrix} \begin{bmatrix} V_s^{a} \\ V_s^{b} \end{bmatrix} \tag{1}$$

In the above equation and all those following, subscripts *'s', 'r',* and *'g'* refer to stator, rotor-side converter, and grid-side converter, respectively. Similarly, superscripts *'s', 'e', and 'r'* indicate stationary, grid-flux oriented, and rotor-oriented reference frames, respectively.

The preceding transform was easily implemented in PSCAD, though the qPLL had to be built and tuned in PSCAD. The component was developed with the aid of [23], [24], [25], and [26]. Figure 9 contains a diagram of the PSCAD qPLL model. The VCO block in the diagram is a voltage-controlled oscillator, and the angle resolver ensures no jumps of 2π occur.

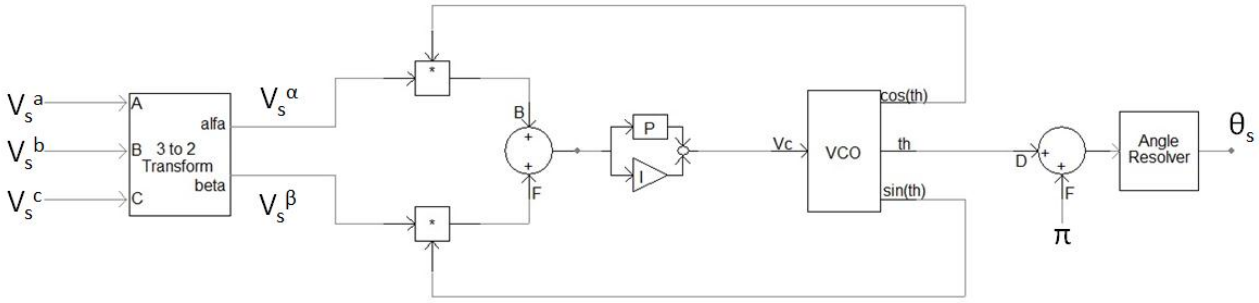

Figure 9: qPLL Developed in PSCAD.

After tuning, the qPLL was correctly configured to generate a signal for the stator flux which was synchronous and in quadrature with the stator/grid voltage vector.

C. Stator-Flux Oriented Frame and RSC

With the synchronization signal, θ_s, the stationary frame-oriented voltage and current signals can be transformed to the grid-flux oriented frame using:

$$\mathbf{V}_s^e = \mathbf{V}_s^s e^{-j\theta_s} \tag{2}$$

$$\mathbf{I}_s^e = \mathbf{I}_s^s e^{-j\theta_s} \tag{3}$$

These new values can then be used to calculate the stator real and reactive power output using:

$$P_s = -1.5 V_{sq} I_{sq} \tag{4}$$

$$Q_s = -1.5 V_{sq} I_{sd} \tag{5}$$

During steady state, the reference real power signal in this thesis is calculated from the wind speed based on a constant tip speed ratio for optimal power extraction. The reference

reactive power signal is specified by the operator and is set to 0 during steady state operation in this study. The calculated real and reactive stator power signals are used along with the command real and reactive power signals to generate real and reactive power mismatch signals, which are sent to PI blocks. The PI blocks are tuned such that their output is used for reference ROF current component signals. During a fault however, the control mode should be switched such that the RSC quickly begins to provide reactive power support. The model adapted from [17] does not provide a reactive power control mode selection algorithm for fault scenarios. The reference rotor current component calculation portion of the controller has therefore been expanded as follows to suit the fault scenario under study.

When the rms voltage of the PCC is at nominal value (within 10% of 1 pu), and the machine is not delivering reactive power, the reference i_{rd}^{r} signal is controlled using the ΔQ_s error signal, as in [17]. However, if PCC rms voltage drops outside the acceptable range, the controller immediately switches to use the ΔV_{rms} error signal to generate the reference i_{rd}^{r} signal. The reference i_{rd}^{r} signal is capped at 1.2pu which is 120% of the rated rotor current. The larger-than-rated current is allowed temporarily during the fault, as suggested by [17]. When this control mode switch occurs, the reference i_{rq}^{r} signal is limited such that the total rotor current magnitude does not exceed 1.2pu. The rotor current control mode returns to normal $\Delta P_s/\Delta Q_s$ control after the PCC rms voltage has recovered to at least 0.9pu and the reactive power injection has returned to nominal.

The GFOF reference rotor current signals are transformed to the ROF using:

$$\mathbf{I_r^r} = \mathbf{I_r^e} e^{j\theta_{slip}} \tag{6}$$

Where θ_s is calculated using:

$$\theta_{slip} = \theta_s - \theta_r \tag{7}$$

The rotor angle is extracted in the machine using a standard encoder. For clarity, the component vectors of the ROF are named *'x'* and *'y'*, rather than *'d'* and *'q'*. These signals are then passed to the VBHCR. The ROF *xy* current components are calculated from the measured three-phase values using Clarke's transform, and these are passed to the VBHCR as well. The VBHCR proposed in [17] uses a 4-level equidistant band hysteresis comparator for the rotor current *x* component error, and a similar 3-level comparator *y* component. The outputs of these comparators, D_x and D_y, are passed to a switching table to look up the RSC switching vector which will be one of six values, as shown in Table 1. These six values correspond to the RSC three-phase switching states, shown in Table 2. For each of the three-phase switching signals, S_a, S_b, and S_c, a value of '0' will result in the phase's low side switch being on and high side switch being off. Conversely, a value of '1' will result in the high side switch being on and the low side switch being off. For more details regarding the development behind this VBHCR, the reader should refer to [17].

Table 1
Switching Table for VBHCR, from **[17]**

		D_y		
		0	1	2
D_x	0	$\mathbf{V}_5$	$\mathbf{V}_4$	$\mathbf{V}_3$
	1	$\mathbf{V}_5$	$\mathbf{V}_0$	$\mathbf{V}_3$
	2	$\mathbf{V}_6$	$\mathbf{V}_0$	$\mathbf{V}_2$
	3	$\mathbf{V}_6$	$\mathbf{V}_1$	$\mathbf{V}_2$

Table 2
Three-Phase Switching States, RSC Output Voltage Vector, and Respective *xy* Components, from [17]

S_a	S_b	S_c	$\mathbf{V}_r$	V_x/V_{dc}	V_y/V_{dc}
0	0	0	$\mathbf{V}_0$	0	0
1	0	0	$\mathbf{V}_1$	2/3	0
1	1	0	$\mathbf{V}_2$	1/3	$1/\sqrt{3}$
0	1	0	$\mathbf{V}_3$	-1/3	$1/\sqrt{3}$
0	1	1	$\mathbf{V}_4$	-2/3	0
0	0	1	$\mathbf{V}_5$	-1/3	$-1/\sqrt{3}$
1	0	1	$\mathbf{V}_6$	1/3	$-1/\sqrt{3}$

D. GSC

As indicated in Figure 8, the GSC control algorithm is very similar to that of the RSC, but simpler. Three-phase GSC current signals are transformed to the stationary frame using Clarke's Transform. In order to calculate the reference GSC current signals, the GFOF *d* and *q* components of the reference GSC current signals are first calculated as follows. The GSC's objective is to maintain DC link voltage, which is coupled to GSC real power, so the error in DC link voltage is fed to a PI controller to generate the *q* component of the reference GSC current signal.

As in the RSC, the *d* component of the reference GSC current signal is calculated using the error in reactive power output. In most control schemes, including those proposed in [17] and [8], the GSC does not contribute reactive power, but [22] proposes an approach that employs the reactive power potential of the GSC for transient scenarios. In this thesis, we will examine the effect of allowing the GSC to contribute reactive power for 1s at fault onset.

The *dq* components of the reference GSC current signal are transformed to the stationary frame using:

$$\mathbf{I}_{\mathrm{g}}^{s} = \mathbf{I}_{g}^{e}\mathrm{e}^{\mathrm{j}\theta_{\mathrm{s}}} \tag{8}$$

The transformed reference signals are then passed to the GSC VBHCR which, aside from the hysteresis comparator bandwidths, is identical to the RSC VBHCR. The GSC VBHCR controls the firing signals of the GSC.

In order to demonstrate successful operation of the developed DFIG controller and LVRT capability, the next section presents simulation results of the test network with no FSIG generation present

V. DFIG FARM LVRT SIMULATION

A. DFIG LVRT without GSC Reactive Power Support

The first simulation run serves to verify functionality of the control scheme presented in [17] for the network at hand and the FERC specification fault scenario. In this setup, the FSIG machine was deactivated, and 1MW of DFIG generation was modeled. The fault scenario initiates at *t=3s*. The following plots illustrate the performance of the designed controller.

Figure 10 shows the real and reactive power output of the DFIG over the duration of the fault. Note that before fault onset, the DFIG is producing constant active power and no reactive power. Upon fault onset, the active power initially rises and then falls as the controller configures the machine to quickly ramp up reactive power output. By the time the fault has cleared, the reactive power output returns to normal, as does the active power output. The fact that the machine remains stable through the fault and also supplies reactive power output indicates that the controller is functioning as desired.

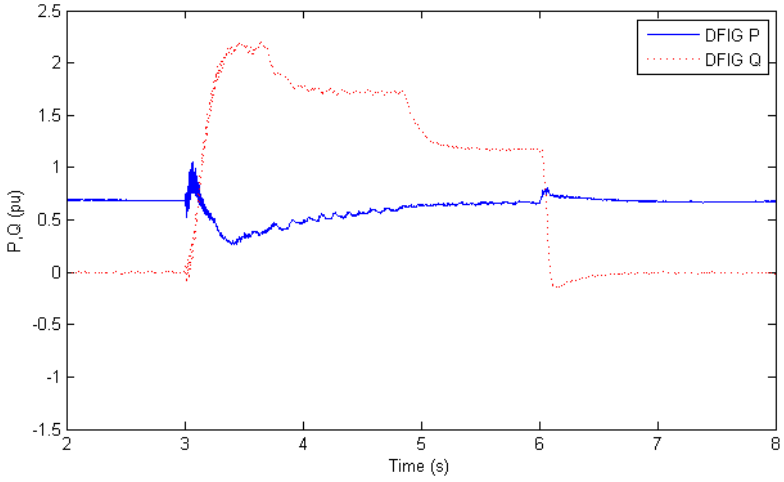

Figure 10: DFIG Real and Reactive Power Output.

In Figure 11, in can be observed that the reactive power output successfully brings the RMS terminal voltage up to 0.9 pu, which is a key factor in maintaining stability through the fault. The voltage spikes during the fault indicate smooth controller response.

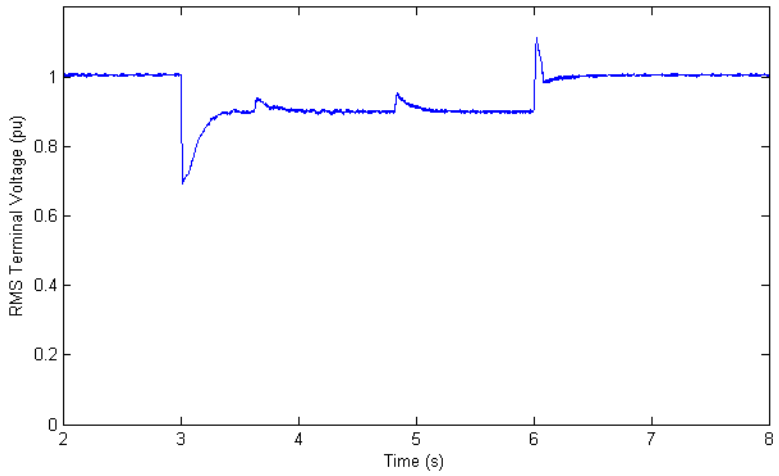

Figure 11: DFIG Terminal Voltage.

The reactive power output and RMS terminal voltage signals from the previous two plots are the signals used to determine reactive power control mode. Figure 12 reproduces these plots along with the reactive power control mode signal. Note the control mode signal has been displaced for clarity. The high value of this signal engages the reactive power control mode described in the previous section. It can be observed that the voltage dip initiates the reactive power control mode. Though the terminal voltage quickly returns to a nominal range, the reactive power control mode does not return to normal while the machine is producing reactive power. This prevents premature control mode switching. Once reactive power and terminal voltage have returned to nominal range, the control mode switches back to standard operation.

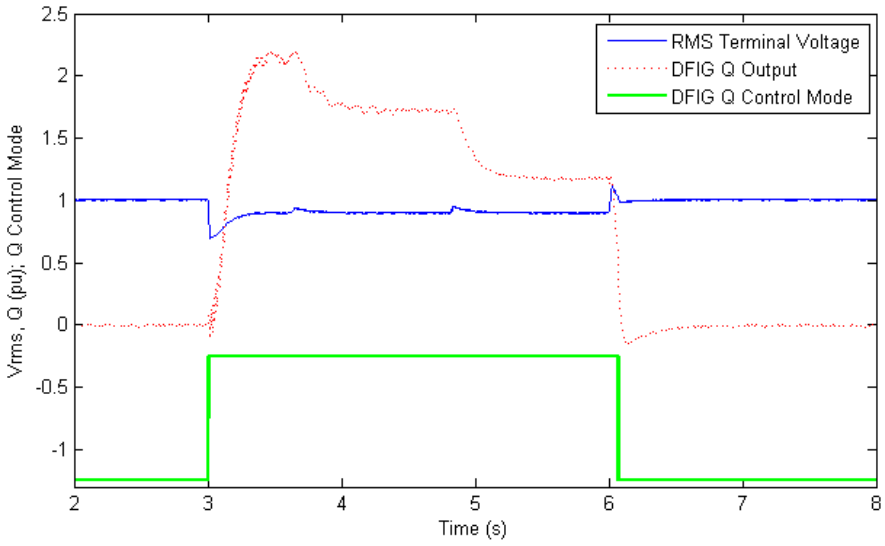

Figure 12: DFIG RSC Reactive Power Control Mode.

While the previous plots indicate successful LVRT performance for the DFIG as well as the desired reactive power control, a major consideration is rotor current and DC link voltage values exceeding their nominal ratings. Figure 13 shows a plot of the rotor current magnitude, and Figure 14 shows the DC link voltage. It can be observed from the first plot that the rotor current only briefly reaches its rated value. This eliminates the need to consider a crowbar type protection device. In addition, the second plot indicates that the GSC is efficiently regulating the DC Link voltage through the transient.

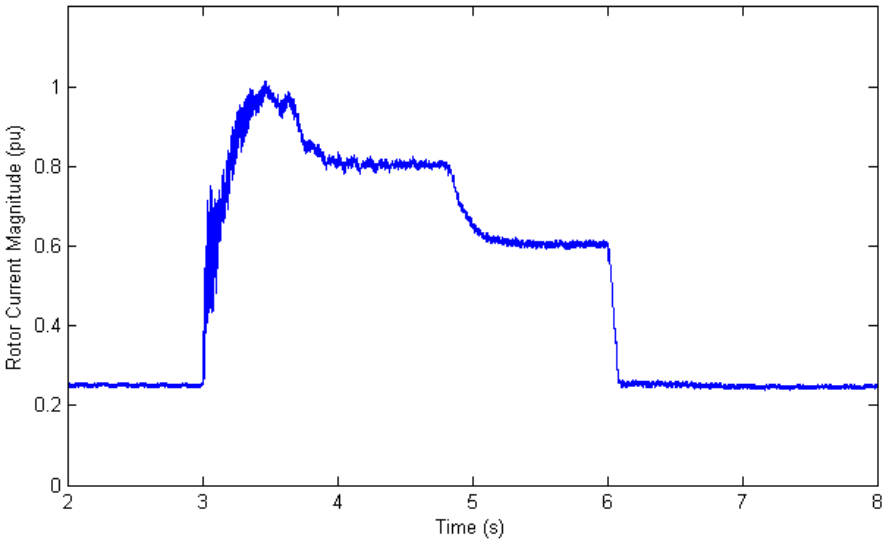

Figure 13: DFIG Rotor Current Magnitude.

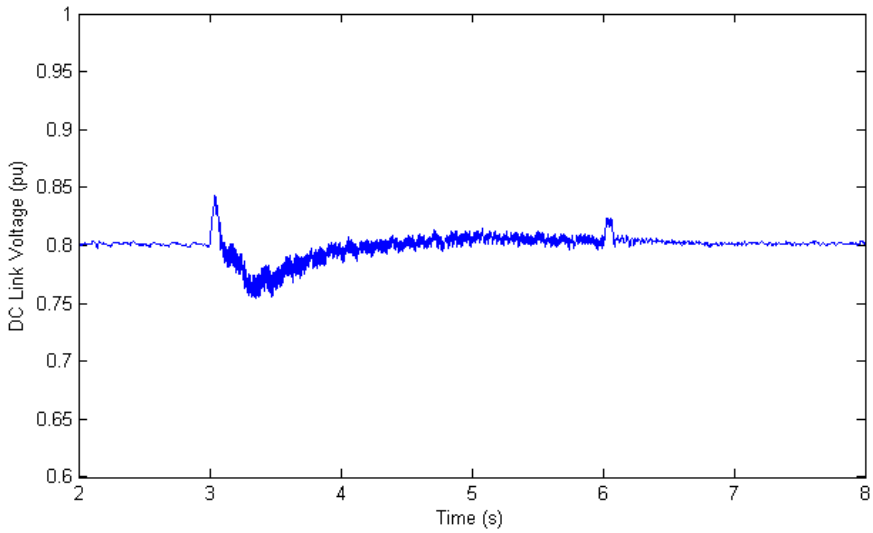

Figure 14: DFIG DC Link Capacitor Voltage.

In order to demonstrate operation of the VBHCR and ROF rotor current control, Figure 15 shows the reference and measured ROF *x* components of the rotor current, which control reactive power. Note the plot only shows waveforms for a period directly around fault onset. Prior to fault onset, the VBHCR is tracking the reference signal with an acceptable error bandwidth. It is possible that the PI controller and VBHCR tuning could further improve this

aspect of control performance. After fault onset, it can be observed that the reduced terminal voltage contributes to transients in the rotor current that the VBHCR has some difficulty overcoming. This transient response is typical in VBHCR controllers and still offers greatly improved response over conventional controllers.

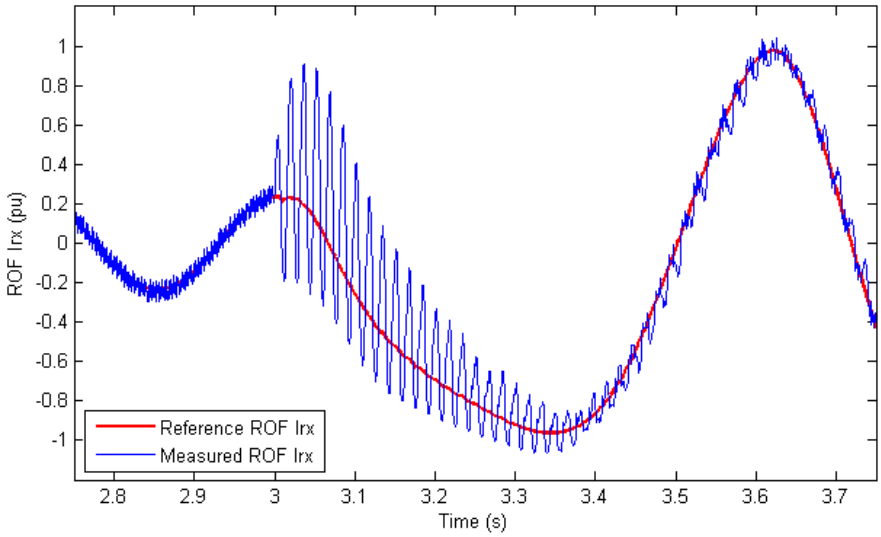

Figure 15: DFIG RSC ROF *x* Component Current.

The preceding plots confirm that the control scheme presented in [17] is applicable for the FERC LVRT standard fault scenario. In the next section, the simulation case is modified by allowing the GSC to contribute reactive power support.

B. DFIG LVRT with GSC Reactive Power Support

In the following scenario, the control scheme was modified as described in Section IV such that at fault onset the GSC briefly delivers reactive power to the grid. Figure 16 shows the PQ and terminal RMS voltage waveforms of this case. These serve to illustrate that the machine still remains stable through the fault and provides reactive power support.

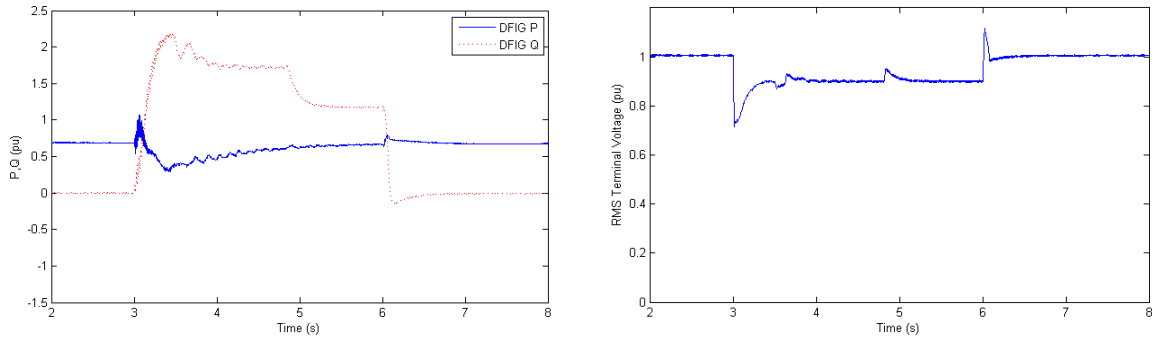

Figure 16: DFIG Real and Reactive Power Output, RMS Terminal Voltage, with GSC Reactive Support Enabled.

The primary motivation for GSC reactive power compensation is increased reactive power support capability without violating rotor current limits. Figure 17 shows that the rotor current magnitude is slightly reduced compared to the case where the GSC does not contribute. This offset could likely be increased if the reactive power limit of the GSC were increased.

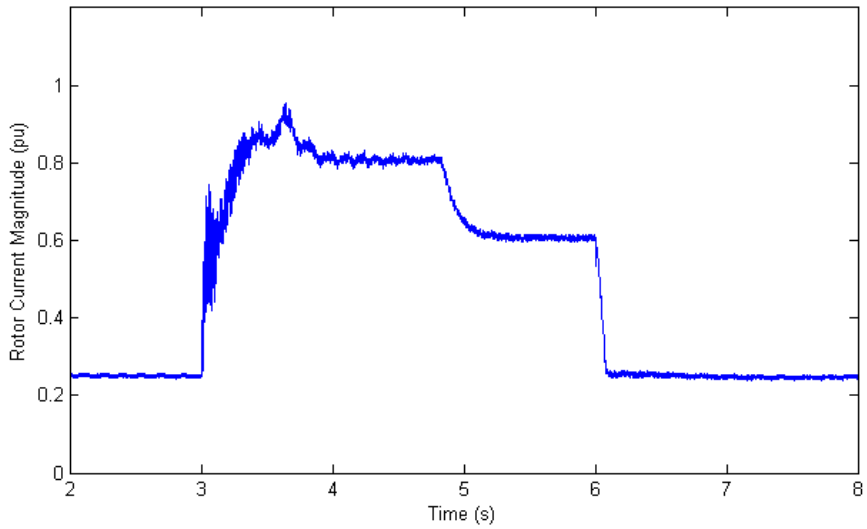

Figure 17: DFIG Rotor Current Magnitude, with GSC Reactive Support Enabled.

Lastly, Figure 18 shows the real and reactive power output of the GSC during the fault. As desired, the GSC rapidly begins to produce reactive power at fault onset. The reactive power output is cut off before the fault is cleared to prioritize maintaining the DC link voltage, and because the RSC easily maintains the terminal voltage after the initial moments of the transient.

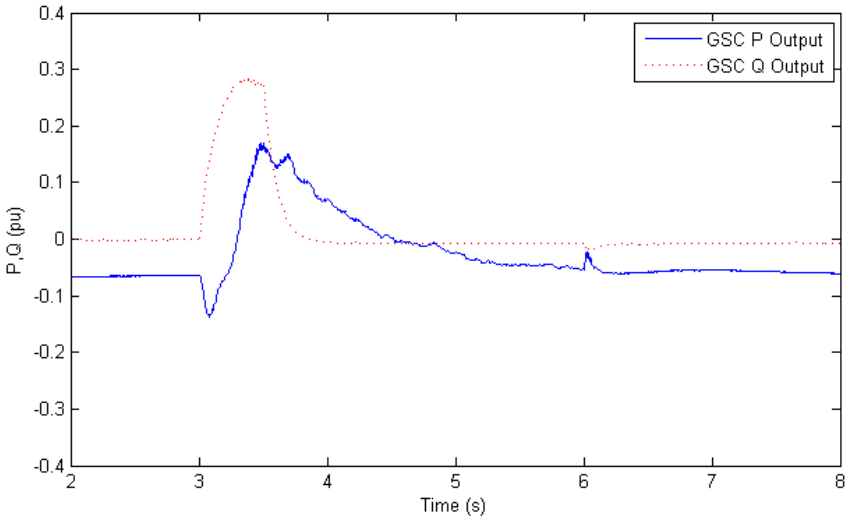

Figure 18: DFIG GSC Real and Reactive Power Output, with GSC Reactive Support Enabled.

The above plots prove that the GSC can be configured to provide a burst of reactive power at fault onset to help the RSC maintain terminal voltage without violating rotor current limits.

VI. HYBRID FARM SIMULATION

This section examines the performance of the developed DFIG controller in providing reactive support for LVRT in hybrid wind farms that also contain FSIGs. In an attempt to ensure LVRT for the aggregate farm, reactive power support from the DFIG is maximized here by allowing GSC reactive support as described in the previous section. In [8], the authors demonstrated capability of DFIGs to provide LVRT capability for adjacent FSIGs, but only with a large ratio of FSIG generation to DFIG generation. Since this thesis aims to explore the practicality of DFIGs as a LVRT solution for FSIGs, the ratio of FSIG generation to DFIG generation was decreased until the DFIG was not capable of supporting the FSIG. First we examine a marginally stable case, and lastly a marginally unstable case.

A. Case with 1MW DFIG and 1MW FSIG

In the first hybrid simulation case, there are equal proportions of DFIG and FSIG generation (1 MW of each). Figure 19 shows the real and reactive power outputs of the DFIG and FSIG machines over the duration of the fault. The first piece to note is that both machines remain stable through the fault and continue delivering real power after fault clearing. Secondly, it can be observed that the reactive power output of the DFIG at fault onset has been greatly increased in comparison to the DFIG-only case. Substantial reactive support is required to maintain the terminal voltage when the reactive power-consumption of the FSIGs is present.

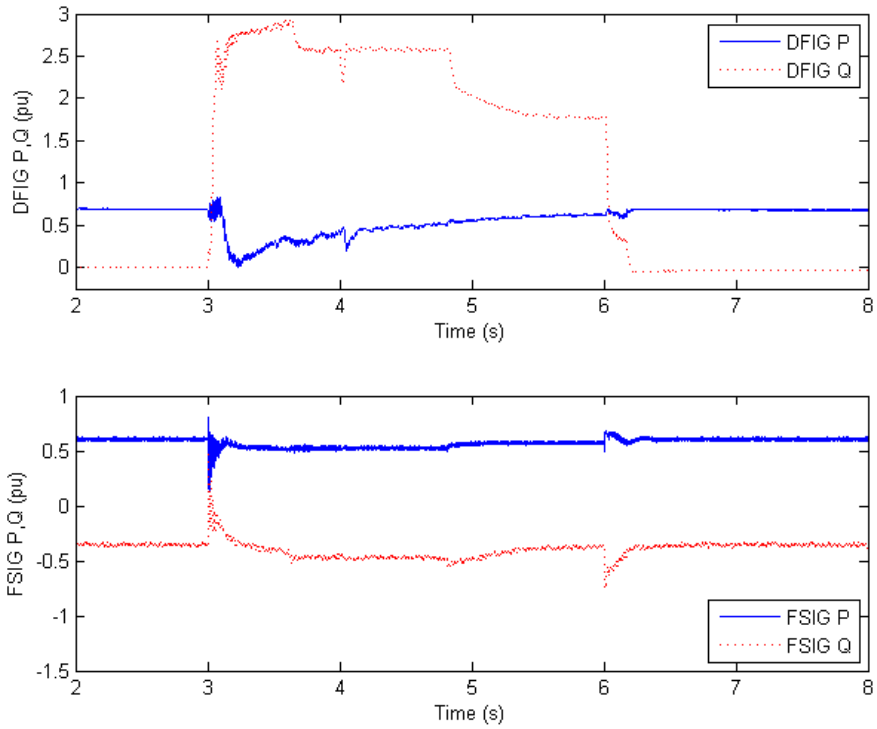

Figure 19: DFIG and FSIG Real and Reactive Power Output with 1MW FSIG Generation.

Figure 20 shows the shaft speed response of the FSIG over the duration of the fault. This plot also indicates that the FSIG is able to stabilize and return to nominal speed after fault clearing with the DFIG's reactive support present. However, referring back to Figure 4, the shaft speed here exhibits the same prolonged leveling off of the marginally stable case in that plot.

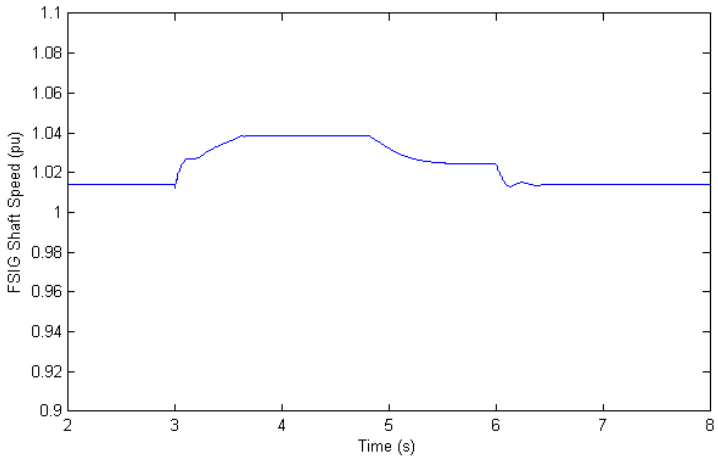

Figure 20: FSIG Shaft Speed with 1MW FSIG Generation.

In order to examine behavior of the two reactive power compensation sources here, namely the RSC and GSC, Figure 21 contains plots for the DFIG rotor current magnitude and GSC power output. From these plots, is it clear that the RSC and GSC are both delivering power at their limits (set in the controller) in order to provide LVRT for the hybrid wind farm.

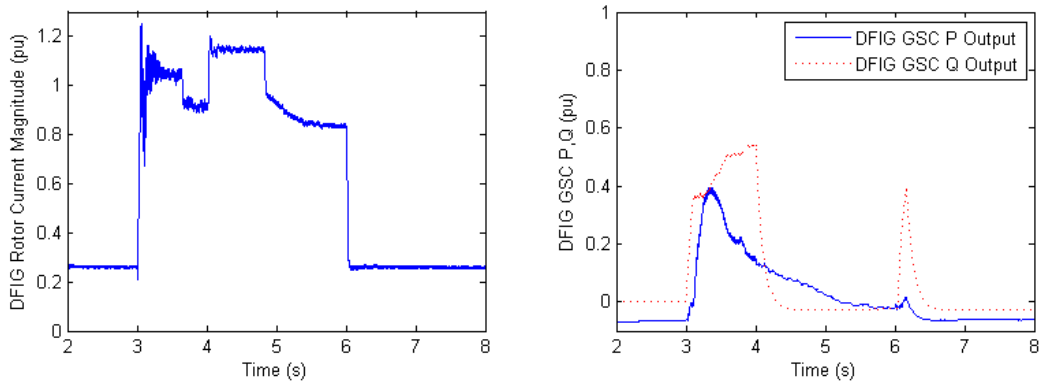

Figure 21: DFIG Rotor Current Magnitude, GSC Real and Reactive Power Output with 1MW FSIG Generation.

B. Case with 1MW DFIG and 1.1MW FSIG

For comparison, the following section relates behavior of the test case with 1 MW of DFIG power generation capacity and 1.1 MW of FSIG capacity. These plots clearly indicate that, even with the GSC providing reactive power, the DFIG is not providing enough total reactive

power to stabilize the larger FSIG machine. By observing Figure 22, it is immediately apparent that the FSIG becomes unstable and stops delivering active power during the fault.

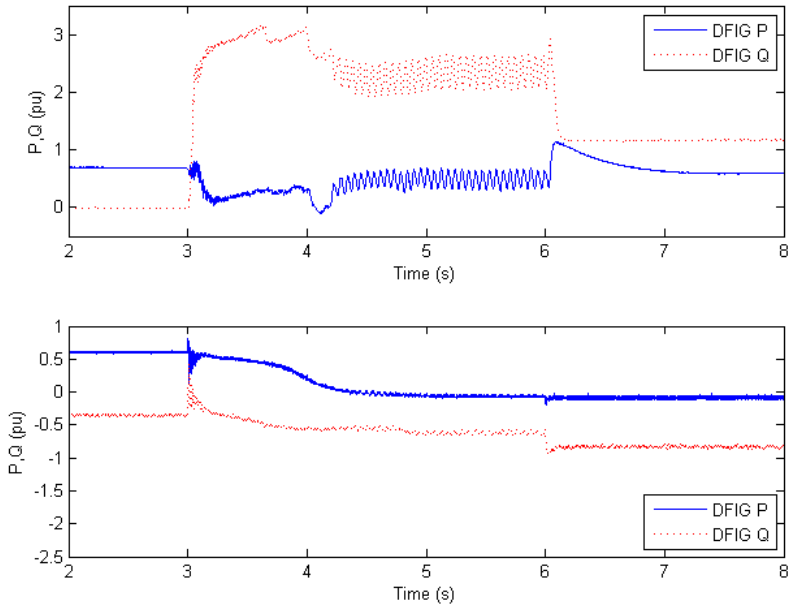

Figure 22: DFIG and FSIG Real and Reactive Power Output with 1.1MW FSIG Generation.

Figure 23 confirms the FSIGs failure to ride through the FERC fault scenario here. Before fault clearing, the machine speed beings increasing at a rate that cannot stabilize.

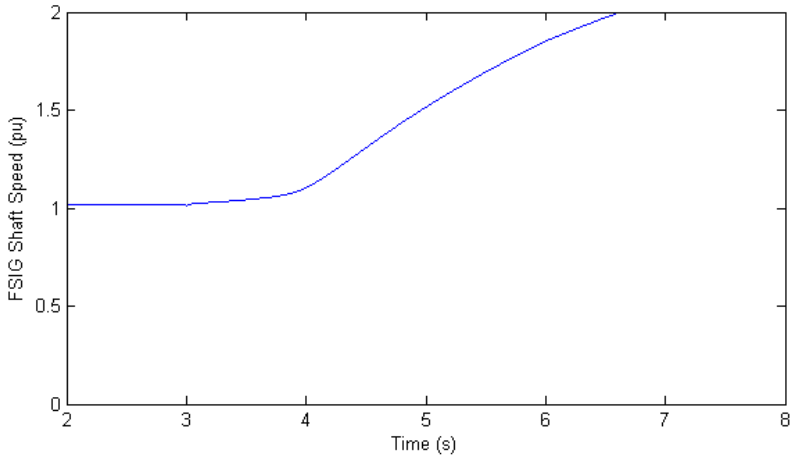

Figure 23: FSIG Shaft Speed with 1.1MW FSIG Generation.

Lastly, Figure 24 shows that the DFIG controller is still working at its limits in an attempt to maintain the terminal voltage.

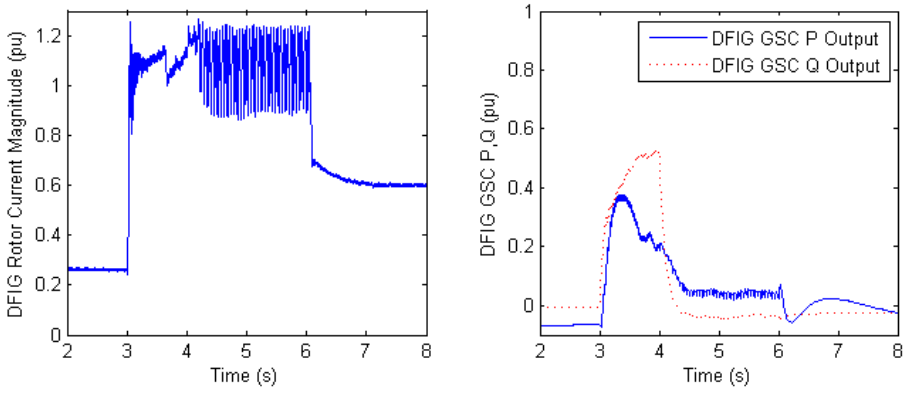

Figure 24: DFIG Rotor Current Magnitude, GSC Real and Reactive Power Output with 1.1MW FSIG Generation.

VII. CONCLUSION

Through time-domain simulation with detailed models, this thesis has demonstrated that the control scheme presented in [17] can be successfully implemented to provide LVRT capability for DFIGs in the fault scenario specified by the U.S. regulator FERC. Building on the grid-flux oriented synchronization and vector-based hysteresis current regulators in this control scheme, it was shown that enabling GSC reactive power support during faults increases LVRT capability of the DFIG. Lastly, it was demonstrated that the expanded control scheme enables DFIGs to provide LVRT in hybrid wind farms for the FERC specification fault, but that this capability is limited with a high ratio of FSIGs in the hybrid farm. In general it appeared that when FSIG generation capacity present is greater than DFIG capacity, the DFIG's reactive compensation potential begins to be insufficient to provide LVRT for the FSIGs. However, many more scenarios should be examined to reach a more complete understanding of this limit. Moreover, adding short-term flexibility to the DFIG rotor current magnitude and GSC reactive power output limits could potentially increase LVRT capability.

Another area of potential future work lies in the modeling of the hybrid wind farm. Due to software limitations and scope considerations this thesis did not examine multiple machine models or trunk/feeder line modeling. These and other wind farm topology dynamics could have significant impact on performance of the proposed LVRT scheme.

VIII. APPENDIX

Transmission Line Impedance Data	
Resistance	2.5Ω
Inductance	0.04H

Transformer Model Data	
Rated Winding Voltages	.69kV/20kV
Positive Sequence Leakage Reactance	0.06 pu
No Load Losses	0.001 pu
Copper Losses	0.002 pu

FSIG Machine Model Data	
Rated Line-Line Voltage	0.69kV
Stator Resistance	0.066 pu
First Cage Resistance	0.298 pu
Second Cage Resistance	0.018 pu
Stator Unsaturated Leakage Reactance	0.046 pu
Unsaturated Magnetizing Reactance	3.86 pu
Rotor Unsaturated Mutual Reactance	0.122 pu
Second Cage Unsaturated Reactance	0.105 pu
Polar Moment of Inertia (J = 2H)	0.85
Mechanical Damping	0.0001 pu

DFIG Machine Model Data	
Rated Line-Line Voltage	0.69kV
Stator/Rotor Turns Ratio	0.3
Stator Resistance	0.0054 pu
Wound Rotor Resistance	0.00607 pu
Magnetizing Inductance	4.5 pu
Stator Leakage Inductance	0.10 pu
Wound Rotor Leakage Inductance	0.11 pu
Polar Moment of Inertia (J = 2H)	0.85
Mechanical Damping	0.0001 pu

Wind Speed & Turbine Data	
Wind Speed	11.5m/s
Air Density	1.225
Power Coefficient	0.28
Rotor Radius	40m

IX. BIBLIOGRAPHY

[1] GE Energy, "Analysis of Wind Generation Impact on ERCOT Ancillary Services Requirements," 2008. December 3, 2012. [Online] Available: http://www.uwig.org/AttchA-ERCOT_A-S_Study_Exec_Sum.pdf

[2] G. Joós, "Wind Turbine Generator Low Voltage Ride Through Requirements and Solutions," in *IEEE Power and Energy Society General Meeting*, 2008.

[3] B. Wu, Y. Lang, N. Zargari and S. Kouro, *Power Conversion and Control of Wind Energy Systems*, John Wiley & Sons, Inc., 2011.

[4] Royal Institute of Technology, Stockholm, Sweden, *Wind Power in Power Systems*, T. Ackermann, Ed., West Sussex: John Wiley & Sons, 2005.

[5] J. D. Rose and I. A. Hiskens, "Challenges of Integrating Large Amounts of Wind Power," in *IEEE Systems Conference*, 2007.

[6] J. Martinez, P. Kjar, P. Rodriguez and R. Teodorescu, "Short Circuit Signatures for Different Wind Turbine Generator Types," in *IEEE Power Systems Conference & Exhibition*, 2011.

[7] E. Vittal, A. Keane and M. O'Malley, "Varying Penetration Ratios of Wind Turbine Technologies for Voltage and Frequency Stability," in *IEEE Power and Energy Society General Meeting*, 2008.

[8] M. Mohseni and S. M. Islam, "Stabilization of Fixed-Speed Wind Generators Using Adjacent Doubly Fed Induction Wind Generators," in *IEEE PES Innovative Smart Grid Technologies Asia*, 2011.

[9] C. D. Le and M. H. Bollen, "Ride-Through of Induction Generator Based Wind Park with Switched Capacitor, SVC, or STATCOM," in *IEEE Power and Energy Society General Meeting*, 2010.

[10] G. Marques and D. M. Sousa, "Understanding the Doubly Fed induction Generator During Voltage Dips," *IEEE Transactions on Energy Conversion,* vol. 27, no. 2, pp. 421-431, 2012.

[11] H. Jadhav and R. Roy, "A Critical Review on the Grid Integration Issues of DFIG Based Wind Farms," in *International Conference on Environment and Electrical Engineering*, pp. 1-4, 2011.

[12] D. Xiang, L. Ran, P. J. Tavner and S. Yang, "Control of a Doubly Fed Induction Generator in a Wind Turbine During Grid Fault Ride-Through," *IEEE Transactions on Energy Conversion,* vol. 21, no. 3, pp. 652-662, 2006.

[13] A. Kasem, "An improved fault ride-through strategy for doubly fed induction generator-based wind turbines," *IET Renewable Power Generation,* vol. 2, no. 4, pp. 201-214, 2008.

[14] M. Rahimi and M. Parniani, "Efficient Control Scheme of Wind Turbines with Doubly Fed Induction Generators for Low-Voltage Ride-Through Capability Enhancement," *IET Renewable Power Generation,* pp. 242-252, 2010.

[15] M. Rahimi and M. Parniani, "Coordinated Control Approaches for Low-Voltage Ride-Through Enhancement in Wind Turbines With Doubly Fed Induction Generators," *IEEE Transactions on Energy Conversion*, vol. 25, no. 3, pp. 873-883, 2010.

[16] N. Aghanoori, M. Mohseni and M. A. Masoum, "Fuzzy Approach for Reactive Power Control of DFIG-Based Wind Turbines," in *IEEE PES Innovative Smart Grid Technologies Asia*, pp. 1-6, 2011.

[17] M. Mohseni, S. M. Islam and M. A. Masoum, "Enhanced Hysteresis-Based Current Regulators in Vector Control of DFIG Wind Turbines," *IEEE Transactions on Power Electronics,* pp. 223-234, 2011.

[18] A. Leon, "An Improved Control Strategy for Hybrid Wind Farms," *IEEE Transactions on Sustainable Energy,* vol. 1, no. 3, pp. 131-141, 2010.

[19] B. Chen, X. Yuan, Y. Xu, X. Wei, Q. Li, R. Sun, J. Song and J. Zhao, "Power Quality Measurement and Comparison Between Two Wind Farms Equipped with FSIG+PMSG and DFIG," in *International Conference on Power System Technology*, pp. 1-7, 2010.

[20] State of Washington Energy Facility Site Evaluation Council, "Wild Horse Wind Power Expansion Project," 2009. [Online] Available: http://www.efsec.wa.gov/wildhorse/Supplemental%20EIS/FSEIS/1-WildHorse%20Final%20SEIS-2009-0109.pdf

[21] "Interconnection for Wind Energy," United States of America Federal Energy Regulatory Commission, 2005. [Online] Available: www.ferc.gov/whats-new/comm-meet/052505/E-1.pdf

[22] W. Qiao and R. G. Harley, "Grid Connection Requirements and Solutions for DFIG Wind Turbines," *IEEE Energy*, pp. 1-8, 17-18 November 2008.

[23] R. D. Christie, "Advanced Power Electronics," 2005. [Private Notes].

[24] V. K. Sood, *HVDC and FACTS Controllers*, Kluwer Academic Publishers, 2004.

[25] B. P. Das, N. Watson and Y. Liu, "Comparative Simulation Study Between Gate Firing Units for HVDC Rectifier Based on CIGRE Benchmark Model," *Energy and Power Engineering,* pp. 120-134, 2011.

[26] M. G. Villalva, M. F. Espindola, T. G. de Siqueira and E. Ruppert, "Modeling and Control of a Three-Phase Isolated Grid-Connected Converter for Photovoltaic Applications," in *Brazilian Power Electronics Conference*, pp. 215-228, 2011.

[27] G. Lalor, A. Mullane and m. O'Malley, "Frequency Control and Wind Turbine Technologies," *IEEE Transactions on Power Systems,* vol. 20, no. 4, pp. 1905-1913, November 2005.

[28] G. Ramtharan, J. Ekanayake and N. Jenkins, "Frequency Support from Doubly Fed Induction Generator Wind Turbines," *IET Renew. Power Gener.*, pp. 3-9, 2007.

[29] I. Erlich and F. Shewarega, "Interaction of Large Wind Power Generation Plants with the Power System," in *First International Power and Energy Conference*, Putrajaya, Malaysia, pp. 12-18, 2006.

[30] B. Wu, Y. Lang, N. Zargari and S. Kouro, *Power Conversion and Control of Wind Energy Systems*, John Wiley & Sons, Inc., 2011.

[31] D. Lorden, K. Clark and E. Larsen, "A Digitally Based HVDC Firing-Pulse Synchronization Control - Description and Module Development," *IEEE Transactions on Power Delivery,* vol. 7, no. 3, pp. 1405-1414, 1992.

[32] M. Mohseni, S. Islam and M. Masoum, "Fault Ride-Through Capability Enhancement of Doubly-Fed Induction Wind Generators," *IET Renewable Power Generation,* pp. 368-376, 2011.

[33] B. Fox, D. Flynn, L. Bryans, N. Jenkins, D. Milborrow, M. O'Malley, R. Watson and O. Anaya-Lara, *Wind Power Integration - Connection and system operational aspects*, London: The Institution of

Engineering and Technology, 2007.

[34] M. Molinas, J. A. Suul and T. Undeland, "Wind farms with increased transient stability margin provided by a STATCOM," in *IEEE Power Electronics & Motion Control Conference*, pp. 1-7, 2006.